Thermo-structural Finite Element Analysis of Direct Laser Metal Deposited Thin-Walled Structures

Srdja Zekovic, Rajeev Dwivedi, Radovan Kovacevic
Research Center for Advanced Manufacturing
Southern Methodist University, 1500 International Pkwy., Suite 100
Richardson, TX, 75081

Abstract

Multilayer direct laser metal deposition is a fabrication process in which the parts are fabricated by creating a molten pool into which particles are injected. During fabrication, a complex thermal history is experienced in different regions of the build, depending on the process parameters and part geometry. The thermal history induces residual stress accumulation in the buildup, which is the main cause of cracking during the fabrication. The management of residual stress and the resulting distortion is a critical factor for the success of the process. A thermo-structural finite element model (FEM) of the process is developed, and the analysis reveals different patterns of residual stress in the thin-walled structures depending on the deposition strategy and the geometry of the structures. The residual stress patterns obtained from finite element analysis (FEA) are in good agreement with the experimental results.

Introduction

One of the most important goals that the modern manufacturing community has been pursuing in the last decades is the reduction of the concept-to-production delay [1]. Research in this area has contributed to the growth of rapid prototyping (RP) and rapid tooling (RT) techniques. The industry is now extending the application of the technology to the new concept of the production of finished goods termed rapid manufacturing (RM) which is believed to overshadow the RP and RT markets [2]. Also, some of these technologies have already been applied successfully in part refurbishment and repair [3].

A few of the RP techniques allow the fabrication of fully dense and metallurgically sound metallic parts, suitable for functional testing and application. The techniques such as direct metal deposition (DMD), laser engineered net shaping (LENS[TM]), and direct light fabrication (DLF) have been used to fabricate the three-dimensional parts of materials such as tool steels, high alloy steels, nickel super alloys, etc.

The multi fabrication (MultiFab) system based on the combination of additive (laser metal deposition and arc welding) and subtractive (milling, drilling and turning) techniques developed at Southern Methodist University is a promising manufacturing system that can be widely applied in solid freeform fabrication (SFF), functionally graded materials (FGM) deposition, component repair and refurbishment, and surface modification. For the SFF application MultiFab

system utilizes a 1-kW continuous wave (CW) mode neodymium-doped yttrium aluminum garnet (Nd:YAG) laser beam to generate a molten pool onto a metal substrate that concurrently moves along a pre-programmed path. At the same time, the additional material in the form of a metal powder carried by inert gas (Argon) is injected into the molten pool. The solidification of the pool after the heat source has passed leaves the additional material fused to the substrate in the form of a bead. Repeating the process on the previously deposited beads as the substrate allows the complex three-dimensional structures to be built directly from the CAD solid model.

Laser-based direct metal deposition (LBDMD) is well suited for the near-net fabrication of intricate individual components like thin-walled structures or small features as parts of larger structures (e.g. die-casting tooling). LBDMD is capable of producing three-dimensional components from many of the commercial alloys. The H13 tool steel is difficult to deposit due to the residual stress accumulation. However, it is material of choice for the die and tool industry [4]. Beside the deformations that lead to dimensional losses, the residual stress accumulation is the biggest cause of cracking during the fabrication of tool-steel components. Basically, residual stress occurs when a body is subjected to a non-uniform temperature change. This stress is usually called thermal stress [5]. Since the laser-metal interaction causes high temperature gradients in the material, the structures fabricated by laser assisted deposition are subjected to high thermal stress. The previous research has revealed that structures fabricated by depositing the H13 tool steel consist predominantly of tempered and non-tempered martensite [4, 6]. The martensite transformation, which is caused by high cooling rate taking place at relatively low temperatures, is an additional cause of residual stress [5, 6, 7, 8].

There is a variety of different techniques that can be used to measure residual stresses like incremental hole drilling, X-ray diffraction, neutron diffraction etc. To reduce the high residual stress some techniques like control heat input, substrate preheating [9,10], heat treatment between subsequent deposition sequences [4], and inductive heating of substrate and buildup [11] have been proposed. In order to choose the appropriate fabrication parameters and apply some of the above mentioned stress relief techniques it would be useful if residual stress values were known in advance. Finite element analysis (FEA) has been confirmed as a powerful numerical simulation tool for stress analysis in welding processes. FEA can be used to predict the residual stress in the laser-based SFF processes.

Some models for laser metal deposition simulations have been developed in the last decade. Most of the models include some approximations in order to avoid long computing time, material and geometrical nonlinearity. Following Dobranich's and Dykhuizen's [12, 13, 14] steady-state analytical and numerical simulations of the LENS^{TM} process with a number of simplifying assumptions, Vasinonta et al. [10] developed a 2D thermo-mechanical model for a thin-walled structure. The thermal model is predominantly conductive, doesn't include the effects of convective and radiative heat transfer from the free surfaces of the wall to the surrounding area, and does not model convective flows in the melting pool itself. The laser heat source is modeled as a point source, neglecting the distribution of the laser power over the molten pool region. The substrate is not explicitly modeled and is represented as a constant temperature boundary condition. The same mesh is used for the thermal as well as for the structural model. The temperature distribution from thermal model is used as the only load. The influence of the substrate is modeled as the displacement constricted to zero. The temperature

dependent thermal and mechanical material properties for stainless steels AISI 304 are used in the model. The model is used to investigate the influence of the process parameters (laser power and velocity, as well as part preheating) on the size of the molten pool and the residual stress distribution in the wall.

Aggarangsi et al. [15] used a similar model to the investigate effects of laser power control on residual stress distribution in a tall thin wall fabricated of stainless steel AISI 316. They modeled two passes of the moving heat source on the top of the wall and compared results qualitatively with the experimental results from Raganswamy's work [16].

Hofmeister et al. [17] developed a 3D thermal FEM using the element birth technique to simulate the LENS^{TM} process. They analyzed the thermal behavior during the fabrication of a thin wall. The model includes conduction as the only mode of heat transfer, where the substrate is held at a constant temperature, and the heat input is modeled by setting the nodes that belong to the elements in the molten pool to the melting or superheat temperatures (in two cases). The material properties were based on generic stainless steel. FEA was used to determine the locations of the thermal gradients with respect to part geometry in order to reduce the distortion and thermal stress in part fabrication.

Labudovic et al. [18] used 3D sequential thermo-structural FEM with the element birth technique to study the heat transfer and residual stress development during the fabrication of a thin wall by laser metal deposition. Also, they analyzed the influence of substrate preheating and heat treatment on the development of residual stresses. The boundary conditions included convection and radiation. The all thermo-physical, as well as thermo-mechanical properties, of the MONEL 400-alloy were considered as temperature dependent. The mean value of the heat flux normal distribution is applied as the thermal load.

In the present work, a new 3D sequentially coupled thermo-structural FEM of direct laser metal deposited thin-walled structures is developed. The element birth technique is used to simulate metal deposition. The purpose of this model is to analyze the heat distribution and its influence on the development of residual stress in thin-walled structures fabricated from H13 tool steel powder by the LBDMD process. This problem typically requires the incorporation of 3D effects. Three cases are studied: a straight wall fabricated by the zig-zag deposition strategy, a straight wall fabricated by the one-direction deposition strategy, and a cylindrical wall fabricated by one-direction deposition strategy. The material model accounts for all highly nonlinear thermo-physical and thermo-mechanical properties and transformations of the material during the process. The residual stress distribution gives explanation for some phenomena observed during the process. Also, some of the results from FEA are qualitatively compared to Raganswamy's experimental results [16].

Modeling Approach

Because of its inherent history dependence, the solution for laser metal deposition requires the transient thermal stress analysis of the entire process that includes deposition and cooling sequences. A coupled thermo-mechanical solution scheme in which the transient heat flow

analysis is integrated with the thermal stress analysis for the elastic-viscoplastic material behavior would be ideal. But the relatively weak thermo-mechanical coupling allows the two-field problem to be solved by staggered procedure which leads to a unidirectional data flow of thermal and mechanical driving forces.

Three-dimensional transient thermal analysis is conducted first to obtain the global temperature history generated during the laser deposition process. A transient stress analysis is then developed with temperatures obtained from thermal analysis entered as loading to the stress model.

A sequentially coupled thermal-stress analysis is commonly used in simulations of welding, laser, and e-beam deposition processes since the rather slow stress development affects very little heat transfer. Such an analysis is not only faster and computationally more economical, but also allows for all the useful features of individual thermal and stress analyses available in the FE packages to be applied.

Heat Flow Analysis

Since LBDMD is a thermal process, the well-known heat conduction plays a central role in the physical modeling of the process. The governing equation for 3D heat conduction (1) follows from the energy balance of an appropriately chosen volume and consists of the diffusive heat flows, and the moving heat source.

$$\rho c \frac{\partial T}{\partial t} = \dot{Q} + k \left[\frac{\partial^2 T}{\partial x^2} + \frac{\partial^2 T}{\partial y^2} + \frac{\partial^2 T}{\partial z^2} \right] + \frac{\partial k}{\partial T} \left[\left(\frac{\partial T}{\partial x} \right)^2 + \left(\frac{\partial T}{\partial y} \right)^2 + \left(\frac{\partial T}{\partial z} \right)^2 \right] \qquad (1)$$

In this relation T [K] is the temperature, $\rho = \rho(T)$ [kg/m^3] is the density, $c = c(T)$ [J/kgK] is the heat capacity, $k = k(T)$ [W/mK] is the heat conductivity, $\dot{Q}(x, y, z, t)$ [W/m^3] is the volumetric heat generation.

The thermal load is applied as a moving volumetric heat source through the molten zone which consists of the material from the substrate (or previous bead) and the injected powder. The beam is assumed to have a uniform power distribution, which is a good approximation since fibre-delivered multi-mode Nd:YAG lasers have an intensity pattern that is essentially flat topped [19, 20]. The absorbed power depends on the losses through the optical fibre (9% of the nominal laser power) and the material absorbtivity at elevated temperatures. For Nd:YAG lasers (1.06μm wavelength) the radiation absorbtivity (*a*) of the steels doesn't change much with the temperature and varies in the range 35-40% [20].

Beside the dominant influence of the heat conduction, the heat loss by forced convection and radiation are included in the thermal analysis and they are incorporated in the model as boundary conditions for specific areas of the structure; i.e. closer or farther from the molten pool. The radiative and convective heat loss from the molten pool to the environment is defined by an empirical relationship as proposed by Goldak [21]

$$h = 2.4 \cdot 10^{-3} \varepsilon T^{1.61} \quad [\text{W/m}^2\text{K}] \qquad (2)$$

where ε is emissivity of the surface of the body. A value of 0.9 was assumed for ε, as recommended for hot rolled steel [21].

The laser metal deposition takes place under intensive flow of inert gas argon from radially symmetric four nozzles. Consequently, the forced convection heat transfer on the wall and substrate surfaces should be considered.

Because of the wide temperature range in the deposited structure, the thermal material properties are clearly nonlinear i.e. the heat capacity and thermal conductivity are temperature-dependent. As the effects of latent heat accompany them, both the phase changes of the material, solid-solid and solid-liquid, are of the particular interest. Since the temperature gradients in the material during the laser-metal interaction are high the solid-solid phase transformation for H13 tool steel is actually a martensitic transformation. In the time-temperature transformation (TTT) diagram for H13 [22] transformation curves are shifted toward higher time values that accounts for the dominant martensitic structure in the H13 deposit.

The latent heat changes during martensitic transformation and solidification take place over finite temperature intervals and can be presented by an equivalent temperature distribution of free enthalpy. Since the enthalpy H [J/kg] and heat capacity c [J/kgK] are related by:

$$\Delta H(T) = \int_{T_1}^{T_2} c(T)dT \tag{3}$$

the latent heat effects of the phase changes can be incorporated in the form of an equivalent increase of the heat capacity.

Thermal Stress Analysis

In a sequentially coupled analysis, the mechanical fields are analyzed proceeding from the already known temperature fields. The quasi-static motion of an elementary volume is governed by the rate form of equilibrium between stress $\dot{\sigma}^t$ and body forces $\dot{p}_v$ (temperature distribution) [23].

$$div\,\dot{\sigma} + \dot{p}_v = 0 \tag{4}$$

The mechanical rate and history effects are affected by the extreme range of temperatures, the high temperature gradients and the large variation of temperature rates. Although uniaxial tension data are available for a large variety of alloys tested at widely different temperatures under steady conditions, there is little information on the effect of thermal transients and thermal gradients on the mechanical response behavior. The traditional decomposition of the mechanical response behavior into uncoupled thermal, elastic and plastic components is a first approximation at best. Generally, plastic behavior should include viscosity for residual stress problems such as multi-pass welding or multilayer direct laser deposition, but in this analysis it is not considered.

The rate form of the total strain $\dot{\varepsilon}$ is composed of the rates for the elastic strain $\dot{\varepsilon}_e$, conventional plastic strain $\dot{\varepsilon}_p$, plastic strain from transformation plasticity $\dot{\varepsilon}_{tp}$, and thermal strain $\dot{\varepsilon}_T$:

$$\dot{\varepsilon} = \dot{\varepsilon}_e + \dot{\varepsilon}_p + \dot{\varepsilon}_{tp} + \dot{\varepsilon}_T \tag{5}$$

Hooke's law applies to the elastic strain and can be subdivided to the deviatoric and dilatoric or volumetric portion.

The combination of yield condition, yield law and hardening law applies to the plastic strain. The yield condition mostly used is von Mises distortion energy hypothesis. The yield law states the plastic strain increment as coaxial and proportional to the deviatoric stress. The isotropic (or also kinematic) work-hardening is represented by the hardening modulus and the effective plastic strain increment.

The thermal strain is given by dilatoric strain components that are function of thermal expansion coefficient.

The transformation-plastic (deviatoric) strain is proportional to the stress. The factor of proportionality depends on the transformation related volume change and yield stress. Therefore, the information relating to thermal expansion coefficient α [1/K] and yield strength σ_Y [MPa] is required at the transformation point where the phase transformation (martensitic transformation) effects exhibit considerable material discontinuities. At the transformation temperature, an abrupt change of α to the negative value occurs, caused by the transformation strain acting in the opposite direction to the thermal strain. Since this plastic anomaly is caused by the second order residual stress resulting from discontinuous distribution of transformation progress in neighboring crystallites, yield stress may be greatly diminished in the temperature range of the transformation.

Experiment

As described in the introduction, three single-bead thin wall samples are fabricated layer by layer. The zig-zag straight wall is fabricated by moving the laser head back and forth during deposition. For the one-directional straight wall, each layer is deposited in the same direction with the fast laser head repositioning between them. During the repositioning laser is off. The cylinder is deposited in a counterclockwise direction.
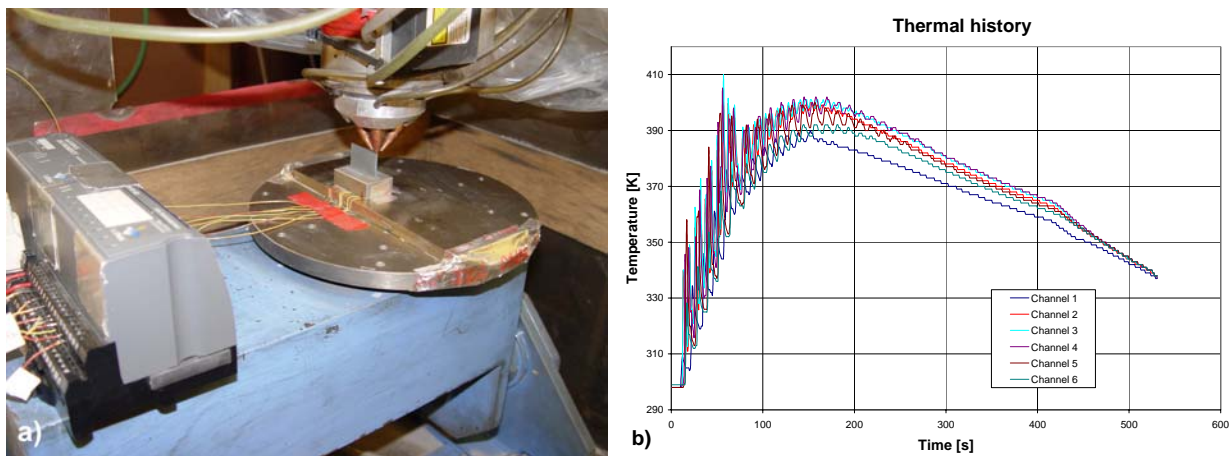

Fig. 1 Experimental set-up a) and thermal history diagram b)

All the samples are fabricated from H13 tool steel powder with a mesh size of -100/+325 (particle sizes between 45 and 150 μm) on the substrates of the same material. The total mass flow rate of the powder is 8 g/min. The cylinder circumference is equal to the length of the straight walls (30 mm). The buildup samples consist of 60 layers. Each layer is 0.325-mm high and 1.1-mm wide. The substrate dimensions are 40x20x6.3 mm. The all deposits are fabricated at the constant nominal laser power of 200 W and the beam traverse speed of 5 mm/s. The first five layers are deposited at a higher laser power in order to attenuate influence of the substrate (or heat sink) proximity and to generate a wall of uniform thickness.

The temperature history, during the deposition process is measured in the substrate at six points, 1mm below the surface. The experimental set-up with the thermocouples and temperature history diagram are presented in the Fig. 1. A satisfying accuracy level in thermal part of the simulation can be achieved by matching the computed thermal histories to the measured thermal histories.

Finite Element Model

The general purpose FE package ANSYS is used for both the thermal and stress analyses performed sequentially with an appropriate combination of elements. The main features of the 3D model are the moving heat input, the element birth-and-death technique, the heat loss, the temperature-dependent material properties, and the application of ANSYS parametric design language (APDL) to model the moving heat source and adaptive boundary conditions.
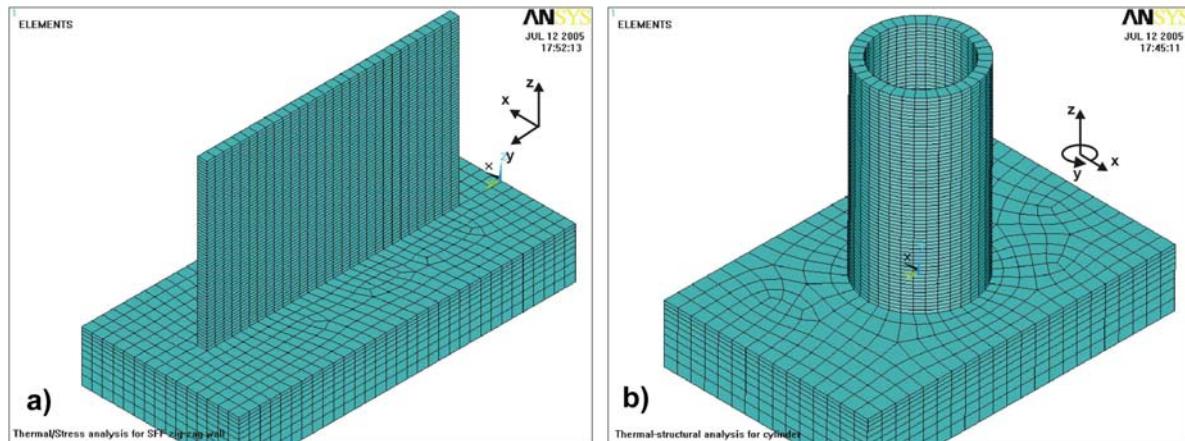

Fig. 2 Straight wall mesh a) and cylindrical wall mesh b)

The element types used in the thermal and structural analyses are SOLID70 and SOLID45, respectively. Both of them are the 8-noded brick elements that are compatible and can be automatically converted to each other during the solution process. The meshes used for both simulations (thermal and structural) are the same, and they are shown in Fig. 2. The straight wall model is created in the Cartesian coordinate system. The x direction is defined as the horizontal coordinate normal to the direction of deposition, the y direction is horizontal coordinate along the direction of deposition, and the z direction is the vertical coordinate (Fig. 2a). The cylindrical wall model is created in the cylindrical coordinate system. x- and y-coordinates are defined as the radial and angular directions, respectively, while the z-coordinate is defined in the vertical direction (Fig. 2b).

344

The moving heat source is modeled by setting a heat generation to the elements of the molten pool zone. The total heat input is evaluated according to the selected type of heat source.

The metal deposition is considered by using the element birth technique. This technique is based on deactivating and reactivating the elements of the molten pool at a prescribed time as the deposition progresses. This is also the 'arrival' time for the heat input for the deposited elements. Consequently, the thermal mass and the heat flow conditions accurately portray the sequential deposition of the material.

As it was mentioned earlier, the boundary conditions include both convective and radiative heat loss. Since only the current outer surface of the partially completed deposit is a convecting or radiating surface at any given time, the boundary conditions are subject to the birth-death option. Also, the boundary conditions depend strongly on the position of the heat source and gas-powder nozzles. A combined radiative-convective heat transfer is localized in the area of the molten pool. A computational fluid dynamics (CFD) model of the gas and metal powder flow, developed in FLUENT, is used to analyze the parameters of the importance for the forced convection heat loss. Fig. 3 shows the velocity contours of the gas flow around the deposited wall.

The heat transfer coefficient is calculated on the basis of the gas velocity and the already deposited wall height [24]. The appropriate boundary conditions are applied on the wall sides in the areas below the nozzles as well as on the other areas of the wall and substrate surfaces that are subjected to the less intensive gas flow (Fig. 4).
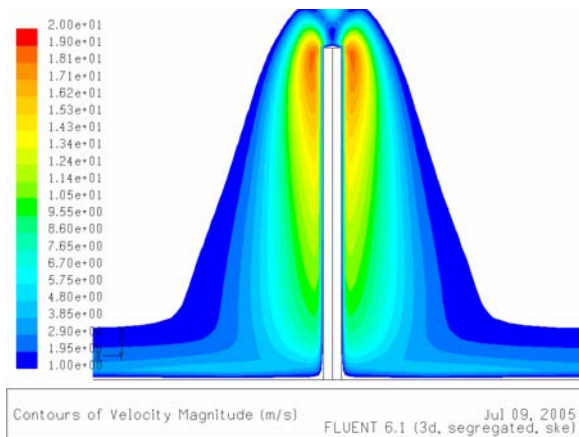

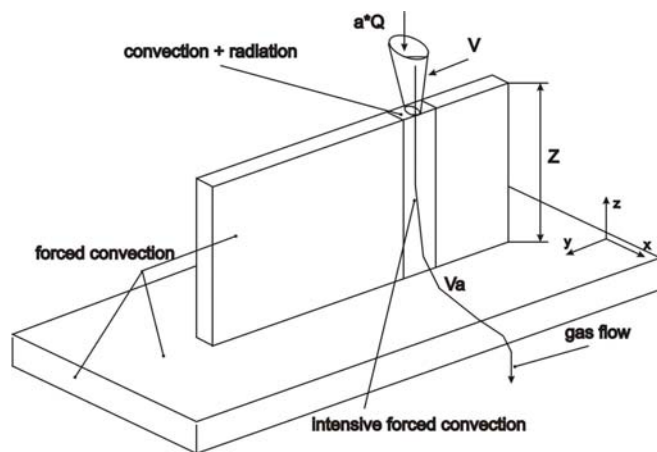Fig. 3   Velocity contours of the gas flow around the wall

Fig. 4   Scheme of the thermal model

The first iteration in the solution procedure solves the system of equations at an assumed starting temperature (298 K), and the subsequent iterations use temperatures from previous iterations to calculate the thermal conductivity and specific heat matrices. The first born element is positioned onto the substrate with a set of initial and boundary conditions. For the subsequent elements, the model uses the results from the previous step as the initial condition for the birth of each new set of elements. This process is repeated for all the birthing events until the geometry is completed. After the structure has been built up the iterative process continues for some time required for the deposit to reach room temperature (the cooling sequence).

Once the thermal simulation is done, the data regarding the temperature distribution in the buildup structure during the process is stored to a database. That data is used in the next step (structural analysis) as the only load that is applied as the body force. The structural simulation consists of the same steps during the building and cooling sequences as in the case of the thermal simulation. So, the temperature distribution scheme from some specific load step in the thermal analysis is applied to the corresponding load step in the structural analysis.

It is necessary to define the boundary conditions in the structural analysis to prevent a rigid body motion. Also, the intention is to allow substrate bending and reduce the influence of the rigid substrate on the stress development in the buildup as much as it possible. For these reasons, displacement of the substrate side surface, perpendicular to the wall depositing direction, is assumed to be zero.

The thermo-physical and thermo-mechanical material properties for H13 tool steel used in this model are acquired from several sources [22, 25]. However, the values for the higher range of temperatures and phase transformations are based on the experimental results, relationships and extrapolation schemes suggested by several authors and in accordance with the previous discussion [7, 8, 9, 21, 23]. In thermo-physical model, the equivalent variation of the heat capacity accounts for the latent heat effects of the ph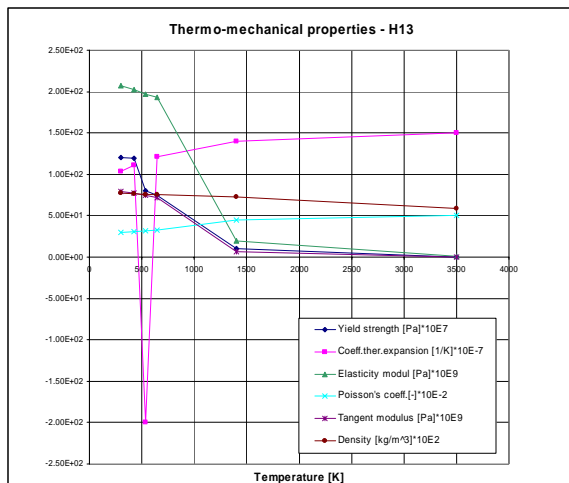ase transformations. In the thermo-mechanical material model, the transformation-induced plasticity is incorporated by the reduction of yield strength, while an equivalent change of the thermal expansion introduces the volume change during the phase transformation. The adequacy of these assumptions is, of course, open to question, and only the experimental determination of the required high temperature data can serve to test its validity.

Fig. 5   Thermo-mechanical properties of H13 tool steel

The bilinear isotropic hardening (BISO) option is used to define the temperature-dependent thermo-mechanical material model in ANSYS. BISO uses the von Mises yield criteria coupled with an isotropic work hardening assumption [26]. The material behavior is described by a bilinear stress-strain curve starting at the origin with positive stress and strain values. This behavior is defined by the elastic modulus E, Poisson's ratio v, the yield strength σ_Y, and the tangent modulus G. The initial slope of the curve is taken as the elastic modulus of the material. At the specified yield stress, the curve continues along the second slope defined by the tangent modulus. It is possible to define up to six (for six temperature values) stress-strain curves, which is not sufficient to describe all the changes of the temperature-dependent material properties in detail. Consequently, some trade off is necessary to define the best approximation avoiding possible ill-behavior of the solution process and thus facilitating convergence. The thermo-mechanical material properties for H13 tool steel are shown in the Fig.5.

Results and Discussion

The transient thermo-structural analysis is performed using boundary conditions and material model discussed in the previous sections, and the process parameters from the experimental part of the work.

Temperature distribution

The maximum transient temperature obtained from thermal analysis at the 41st layer is plotted in Fig. 6. The building of the 41st layer starts at 240 s and finishes at 246 s, counting time from the beginning of the buildup. The temperatures in the molten pool are considerable higher than the melting temperature. They are comparable with some experimental results obtained under similar processing conditions [6, 19, 27].

Also, the thermal contours are in agreement with experimentally obtained thermal contours as seen from the side of the wall [16]. Performing zig-zag laser metal deposition along the top of the straight wall with constant laser power and traverse speed, the thermal contours reach a steady state distribution. When a free edge of the wall is approached, the molten pool size becomes larger, penetrating deeper into the wall. There are two reasons for this: the first is related to the volume decrease of the heat sink close to the free edge, and the second is related to the reduction of the laser velocity (so, increase of heat input to the wall per distance moved in deposition direction) because of the change of the moving directions (reverse) in order to continue deposition in the next layer.
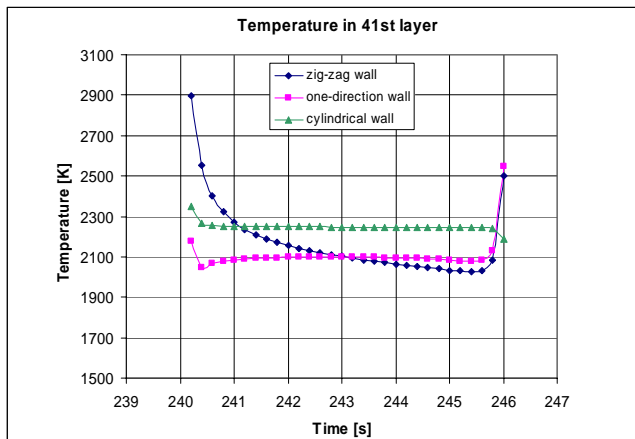

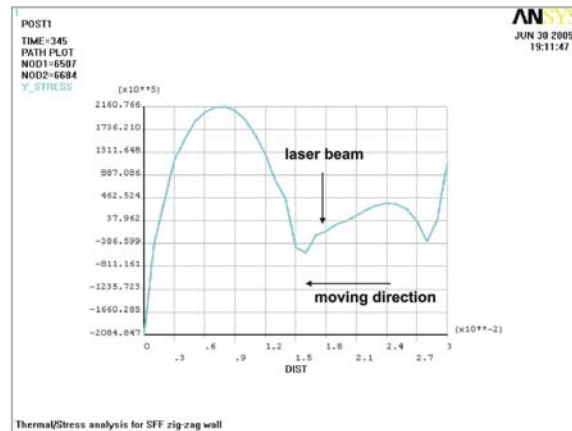Fig. 6 Maximum temperatures in molten pool

Fig. 7 σ_y-stress development during deposition of the 57th layer

In case of the one-direction deposited wall, the increase of the molten pool at the free edges is less pronounced since there is no laser reverse. Instead of that the laser beam is repositioned at high speed from the end to start point. As the result, the heat input is lower at the free edges.

Since the cylindrical wall doesn't have free edges, the temperature distribution is different than in case of the straight wall. That difference means that the higher average temperature is present along the circular path. Also at the start-end point of each layer, the laser beam dwells for some

347

short time during the *z*-direction incremental movement. At that time, the heat input per distance moved along the wall length is increased, and the molten pool penetrates deeper into the previous deposit. Consequently the temperature is higher, but it is still lower than at the straight wall's free edges because of the larger volume of the heat sink.

Stress analysis

The material during laser deposition is subjected to inhomogeneous thermal expansion and contraction that causes specific distribution of the active stress. Fig. 7 shows distribution of the stress σ_y on the top of the 56th layer during the deposition of the 57th layer. Because the molten metal will not support a load, the stress underneath the laser beam is close to zero. As a consequence of the thermal expansion during the heating, a plastic compression zone occurs ahead of the beam (or the molten pool), and as a result of the thermal contraction during cooling, a plastic tensile zone occurs behind the molten pool. Also farther ahead in front of the compression zone, there is a plastic tensile zone as a result of the stress development during the deposition of the previous layer. These zones are separated by a strip with elastic loading from the tensile state into the compression state.

After the deposition and cooling sequences, the inhomogeneous temperatures disappear and so does the elastic thermal stress. The stress that remains is residual stress. Since the residual stress is not measured, some of the FEA results will be qualitatively compared with Rangaswamy's results [16]. The observations from our experiments and the stress patterns will be discussed.

Distribution of the stress σ_z in the *zig-zag deposited wall* in Fig. 8a shows very localized high tensile stress values at the corners. The values are above the tensile strength for H13 tool steel [22], which confirms the crack appearance in the deposit (Fig. 8b). During the deposition, a crack appears first at one of the corners, which causes the stress relaxation in the wall close to the substrate.
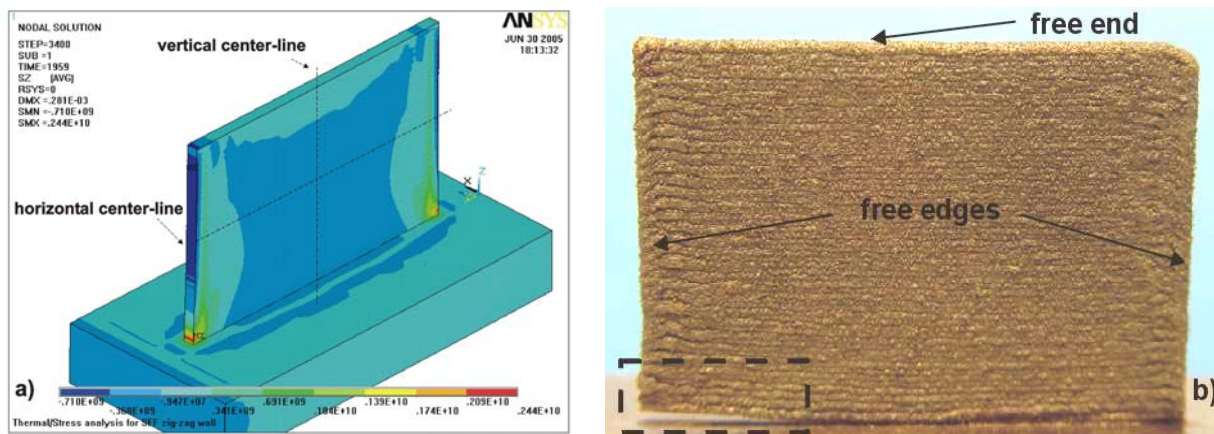

Fig. 8   Residual stress σz in the zig-zag deposited wall a); single bead zig-zag deposited wall b)

Figs 9a and 9b show three residual stress components (σ_x, σ_y, and σ_z) along the vertical center-line, and along the horizontal center-line (the 30th layer) respectively. They can be

compared with the stress obtained by neutron diffraction in Fig. 10a and Fig. 10b [16], keeping in mind that the measurement was performed on a wall of a different size (90mm) and material (stainless steel AISI 316). In all diagrams that represent stress distribution in vertical z-direction abscissa is directed from the free end to the substrate.

The stress distribution in the vertical direction (Fig. 9a) shows that the compressive stress σ_z is increasing toward the substrate while the stress σ_x is almost zero, which is in good agreement with the stress distribution shown in Fig. 10a. At first glance, there is a huge difference in the distribution of the stress σ_y. But, it can be seen that σ_y bellow the free end and close to the bottom of the wall is high, while it is converging to zero toward the center of the wall, which is in agreement with experimental results shown in Fig 10a. This result means that the stress close to the free end is uniaxial in y-direction and the stress close to the substrate is very complex in nature. Obviously, the σ_y in the central part of the wall is affected by the close proximity of the free end and substrate (wall height is 19.5mm).
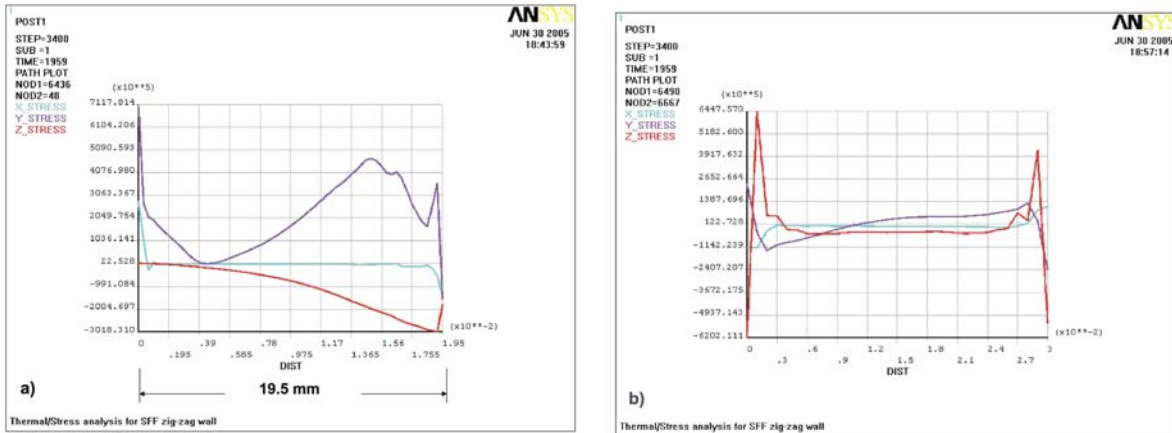

Fig. 9   FEA for zig-zag deposited wall; residual stress distribution along the vertical center-line a), and the horizontal center-line b)
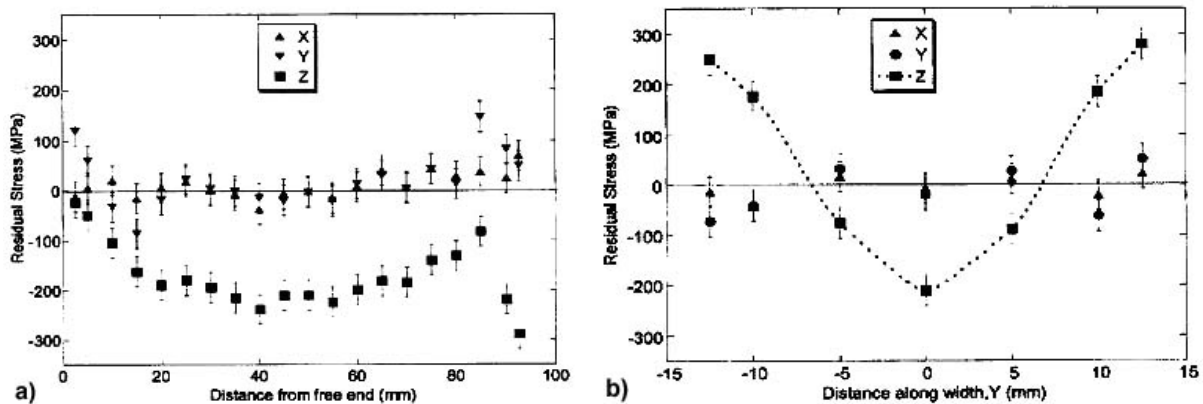

Fig. 10 Results obtained by neutron diffraction for zig-zag deposited wall; stress distribution along the vertical center-line a), and the horizontal center-line b) [16]

The stress distribution in the horizontal direction (Fig 9b) is in good agreement with the experimental results shown in Fig 10b. The stress and moment balance are satisfied by the

distribution of the tensile and compressive stress along the y-direction. The σ_z is dominant and compressive in the center while it turns to a tensile stress in close proximity of the free edge. A possible source of the tensile σ_z in the plot is the constraint from the stiff base plate preventing a bending deformation in the wall [15]. This tensile stress is increasing toward the substrate where it represents the main component stress in the region of the crack appearance (see Fig. 8a). However, this analysis shows compressive stress on the free edges farther from the substrate. This result can be a consequence of the active stress development during deposition explained above (Fig. 7). While the laser beam is dwelling at reverse point for a short time the heat is penetrating deeper into the deposit and, consequently, the molten pool is extended in negative z-direction. The material below the molten pool on the free edge is experiencing compressive stress. Since the laser beam is reverses, the material on the free edge doesn't unload elastically into the tensile stress and stays compressed.
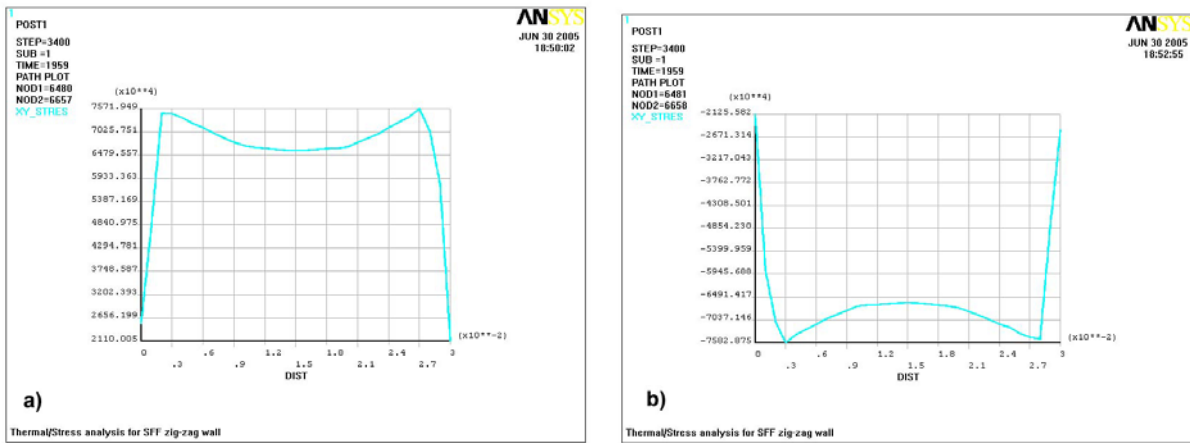

Fig. 11 Distribution of the residual shear stress σ_{xy} along the horizontal center-line: the 30th layer a), and the 31st layer b)
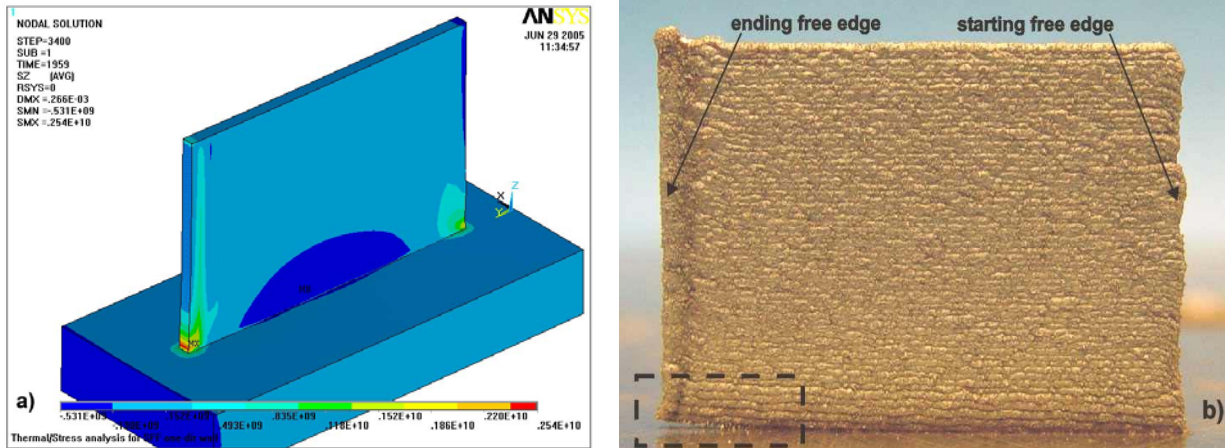

Fig. 12 Residual stress σ_z in the one-directional deposited wall a) and the single bead one-directional deposited wall b)

The stress analysis through the structure of the zig-zag deposited wall reveals the opposite sign of shear stress σ_{xy} in two subsequent layers (Fig. 11a,b) which is not the case in the one-

directional deposited wall, where shear stress is of the same sign in the subsequent layers. It is obvious that the deposition strategy has an influence on the shear stress development.

Generally speaking, the *one-directional deposited wall* has stress values slightly lower than the zig-zag deposited wall which is expected according to lower temperature differences during deposition (Fig. 6). Also, the high localized stress above the tensile strength observed at the corners (Fig.12a), causes cracks (Fig. 12b). Because of the deposition strategy, the stress close to the free edges is not symmetric with respect to the vertical central line as was the case of the zig-zag deposited wall. The tensile stress is higher at the ending free edge (Fig. 12). The stress distribution along the central vertical and horizontal lines is similar to the stress distribution in the zig-zag deposited wall.
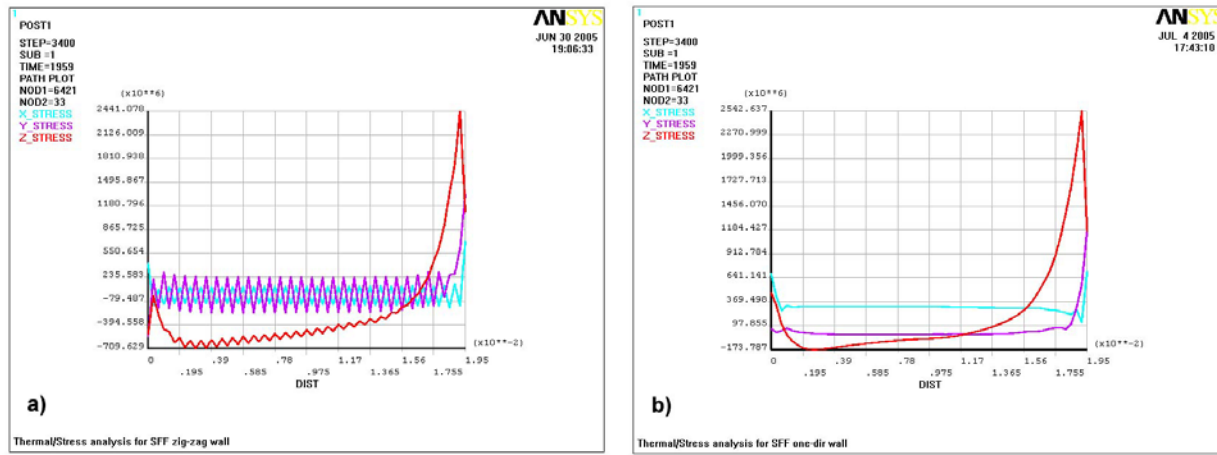

Fig. 13 Residual stress along the ending free edge in zig-zag deposited wall a) and
one-directional deposited wall b)

Some differences of the stress distribution between the zig-zag and one-directional deposited walls can be observed at the free edges. Since, there is no laser beam reverse in the one-direction deposition strategy, the compressive stress in the *z*-direction has lower values, and the stress components σ_x, σ_y, and σ_z in the subsequent layers are of the same sign (Fig. 13a,b). The shear stress σ_{xy} in the subsequent layers is of the same sign, as was mentioned before.
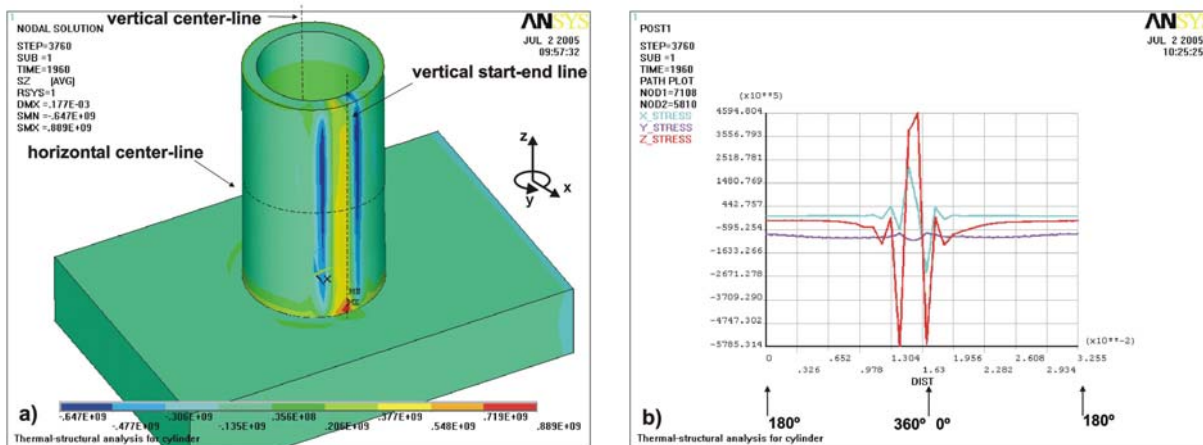

Fig. 14 Residual stress σ_z in cylindrical wall a), and stress distribution along the horizontal-center
line (the 30th layer) b)

351

According to the temperature distribution during the layer deposition presented in Fig. 6, the lower residual stress is expected more in the *cylindrical wall* than in the straight wall, which is proved by the analysis. The maximum residual stress is obtained at the bottom of the cylinder and the value is lower than the material yield strength (Fig. 14).

The stress distribution along the horizontal-central line (the 30th layer) shows pretty uniform values except in the area around the start-end position. In Fig. 14b the start-end point (y=0º) is located in the center of the diagram in order to get a better picture of the stress distribution in the area of interest. The laser beam slows down, at the start-end point, performs incremental movement along z-axis and continues moving counterclockwise in the next layer. This movement induces a non-uniform stress distribution (sharp transition from tensile to compressive stress) whose effect can be recognized on the cylinder surface (Fig. 15).
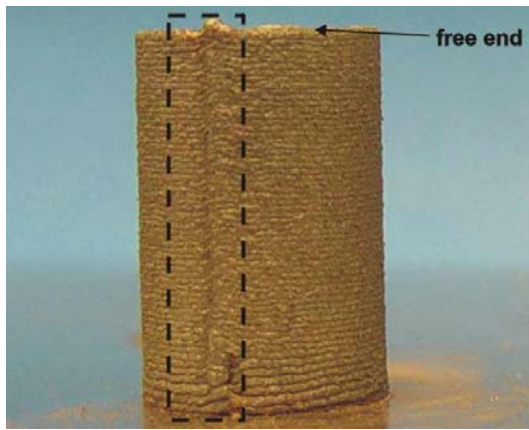

Fig. 15 Single bead cylindrical wall with the 'seam' feature that corresponds to the vertical start-end line

The stress distribution along the vertical central line (y=180º) at the inner surface is uniform except at the free end and the bottom of the cylinder where the stress behavior is complex (Fig. 16a). If this result is compared with the stress distribution along the same line at the outer surface (Fig. 16b), that is also uniform, it is obvious that the axial stress σ_z and hoop stress σ_y at the inner surface is tensile while the stress at the outer surface is compressive. The radial stress σ_x across the thickness of the wall changes the sign too, but it is much lower than the axial and hoop stress. Such distribution of the stress causes a bending effect across the wall thickness.
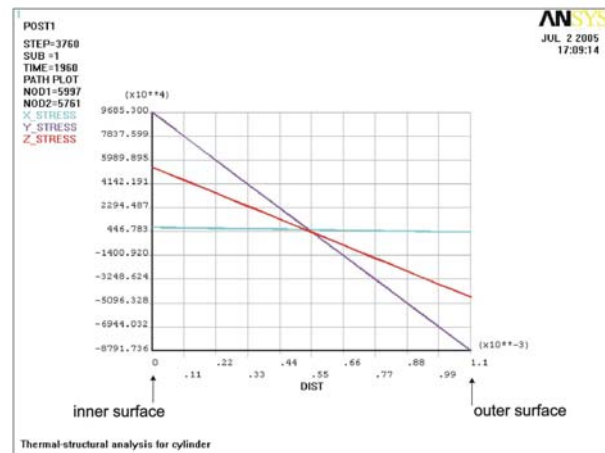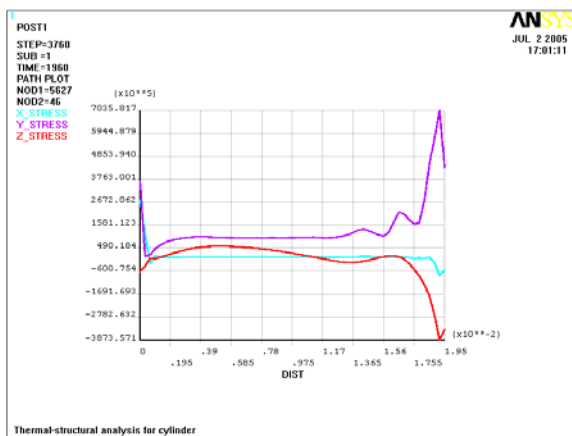

Fig. 16 Cylindrical wall - Residual stress along the vertical center line (180º from start point) a), and residual stress across the wall thickness in the 40th layer (180º from start point) b)

Conclusions

A three-dimensional thermo-mechanical model of the LBAM process has been developed using finite element method of analysis. This approach has been shown to be a powerful tool both for determining the laser deposition thermal cycle as well as for evaluating the stresses as a result of the temperature transients. The major findings are summarized as follows:

a) The straight wall structures are exposed to high tensile residual stress close to the free edges. The residual stress in the contact zone between the wall and the substrate causes cracks at the corners. From the other side, the compressive stress is revealed on the free edges farther from the substrate.

b) The zig-zag deposition strategy induces the residual shear stresses of the different sign in the subsequent layers. In the one-directional deposited wall the residual stress is slightly lower than in the zig-zag deposited wall, but the overall quality of the fabricated structure is lower.

c) Generally, distribution of the residual stress in the cylindrical wall is more uniform than in the straight wall. The residual stress values are much lower and any cracks are not observed. It is a consequence of the more uniform temperature distribution in the cylindrical wall. However, the residual-stress distribution in the cylindrical wall causes bending effect across the wall thickness.

d) 3D finite element analysis helps to identify residual-stress distribution and find critical regions in the structure for different processing parameters. Using this analysis it could be possible to propose optimal the LBDMD process parameters for particular part geometry.

Acknowledgment

REFERENCES

1. Mazumder, J., Dutta, D., Ghosh, A.,and Kikuchi, N., Designed Materials: what and how, Proc. SPIE, 2003, Vol.4831, pp.505-516
2. Wohlers, T., Wohlers Report – Rapid Prototyping, Tooling & Manufacturing State of the Industry, 2003, Wohlers Associates Inc., Colorado
3. Malin, V., Johnson R. N.,and Sciammarella F., Laser Cladding Helps Refurbish US Navy Ship Components, The AMPTIAC Quarterly, 2005, Vol.8, No.3, pp.3-9
4. Mazumder, J., Choi, J., Nagaratham, K., Koch, J.,and Hetzner, D., The Direct Metal Deposition of H13 Tool Steel for 3-D Components, JOM, May 1997, Vol.49, No.5, pp.55-60
5. Masubuchi, K., Analysis of Welded Structures - Residual Stresses, Distortion, and their Consequences, Pergamon Press, 1st edition, London, 1980, ISBN 0-08-022714-7
6. Hofmeister, W., Griffith, M., Ensz M., and Smugersky J., Solidification in Direct Metal Deposition by LENS Processing, JOM, Sep 2001, Vol.53, No.9, pp.30-34

7. Radaj, D., Heat Effects of Welding; Temperature Field, Residual Stresses, Distortion, Springer-Verlag, New York, 1992, ISBN 0-387-54820-3

8. Goldak, J., Bibby, M., Moore, J., House, R., and Patel, B., Computer Modeling of Heat Flow in Welds, Metallurgical Transactions B, Vol.17B, September 1986, pp.587-600

9. Ready, J.F., LIA Handbook of Laser Materials Processing, 1st edition, Laser Institute of America, Orlando, 2001, ISBN 0-912035-15-3

10. Vasinonta, A., Beuth, J.L., and Griffith, M., Process Maps for Controlling Residual Stress and Melt Pool Size in Laser-Based SFF Processes, SFF Symposium, Austin, August 2000, pp. 200-206

11. Ader, C., Brosemer, M., Freyer, C.,Fricke, H., Hennigs, D., Klocke, F., Kühne, V., Meiners, W., Over C., Pleteit, H., Stührmann, S., Wirth I., Wirtz, T. and Wissenbach K., Research on Layer Manufacturing Techniques at Fraünhofer, SFF Symposium, Austin, August 2004, pp.26-37

12. Dobranich, D. and Dykhuizen, R. C., 1998a, "Scoping Thermal Calculation of the LENS™ Process," Sandia National Laboratories Internal Report, 1998.

13. Dobranich, D. and Dykhuizen, R. C., 1998b, "Analytical Thermal Models for the LENS™ Process," Sandia National Laboratories Internal Report.

14. Dykhuizen, R. C., and Dobranich, D. 1998, "Cooling Rates in the LENS™ Process," Sandia National Laboratories Internal Report

15. Aggarangsi, P., Beuth J.L., and Griffith M., Melt Pool Size and Stress Control for Laser-Based Deposition Near a Free Edge, SFF Symposium, Austin, August 2003, pp.196-207.

16. Rangaswamy, P., Holden, T.M., Rogge, R.B. and Griffith, M.L., 2003, "Residual Stresses in Components Formed by the Laser-Engineered Net Shaping (LENS™) Process," The Journal of strain analysis for engineering design, Vol.38, No.6, November 2003, pp. 519-527.

17. Hofmeister, W., Wert, M., Smugersky, J., Philliber, J.A., Griffith, M., and Ensz, M., Investigating Solidification with the Laser-Engineered Net Shaping (LENS™) Process, JOM, Vol.51, No.7, July 1997, http://www.tms.org/pubs/journals/JOM/9907/Hofmeister /Hofmeister-9907.html

18. Labudovic, M., Hu, D., and Kovacevic, R., A three dimensional model for direct laser metal powder deposition and rapid prototyping, Journal of Material Science, Vol.38, 2003, pp.35-49

19. Pinkerton, A.J., and Li, L., An analytical model of energy distribution in laser direct metal deposition, Proc. Instn Mech. Engrs. Vol.218, Part B: J. Engineering Manufacture, 2004, pp.363-374

20. Steen, W.M., Laser Material Processing, 3rd edition, Springer-Verlag, London, 2003, ISBN 1-85233-698-6

21. Goldak, J., Chakravarti, A., and Bibby M., A New Finite Element Model for Welding Heat Sources, Metallurgical Transactions B, Vol.15B, June 1984, pp.299-305

22. International Mold Steel Inc., Premium H13, http://www.moldsteel.com/h13.htm

23. Argyris, J.H., Szimmat, J., and Willam K.J., Finite Element Analysis of Arc-welding Process, Numerical Methods in Heat Transfer, Volume III, Edited by R.W. Lewis, John Wiley & Sons Ltd., 1985

24. Holman J.P., Heat transfer, 7th edition, McGraw Hill Book Company, New York, 1990.

25. Brooks, J., Robino, C., Headley, T., Goods, S., and Griffith M., Microstructure and Property Optimization of LENS™ Deposited H13 Tool Steel, SFF Proceedings, Austin, 1999, pp. 375-382

26. ANSYS Theory Manual, Release 8.1, ANSYS Inc., USA, 2004
27. Smurov, I., Martino, V., Ignatiev, M, and Flamant, G., On-line thermocycles in laser applications, Journal de Phisique IV, Colloque C4, supplement au Journal de Physique III, Volume 4, April 1994, pp.147-150